The Journal of Chemical Physics

RESEARCH ARTICLE | MARCH 06 2025

Enhanced photoisomerization with hybrid metallodielectric cavities based on mode interference

Anael Ben-Asher ; Thomas Schnappinger ; Markus Kowalewski ; Johannes Feist

J. Chem. Phys. 162, 094308 (2025)
https://doi.org/10.1063/5.0252988

The Journal of Chemical Physics ARTICLE pubs.aip.org/aip/jcp

Enhanced photoisomerization with hybrid metallodielectric cavities based on mode interference

Cite as: J. Chem. Phys. 162, 094308 (2025); doi: 10.1063/5.0252988
Submitted: 13 December 2024 • Accepted: 17 February 2025 •
Published Online: 6 March 2025

Anael Ben-Asher,[1,a] Thomas Schnappinger,[2,b] Markus Kowalewski,[2,c] and Johannes Feist[1,d]

AFFILIATIONS

[1] Departamento de Física Teórica de la Materia Condensada and Condensed Matter Physics Center (IFIMAC), Universidad Autónoma de Madrid, E28049 Madrid, Spain
[2] Department of Physics, Stockholm University, Albanova University Centre, SE-106 91 Stockholm, Sweden

[a] **Author to whom correspondence should be addressed:** anael.benasher@uam.es
[b] **Electronic mail:** thomas.schnappinger@fysik.su.se
[c] **Electronic mail:** markus.kowalewski@fysik.su.se
[d] **Electronic mail:** johannes.feist@uam.es

ABSTRACT

The ability to control chemical reactions by coupling organic molecules to confined light in a cavity has recently attracted much attention. While most previous studies have focused on single-mode photonic or plasmonic cavities, here we investigate the effect of hybrid metallodielectric cavities on photoisomerization reactions. Hybrid cavities, which support both photonic and plasmonic modes, offer unique opportunities that arise from the interplay between these two distinct types of modes. In particular, we demonstrate that interference in the spectral density due to a narrow photonic mode and a broad plasmonic mode that are coupled to each other enables hybrid cavities to provide an energy-selective Purcell effect. This effect enhances electronic relaxation only to the desired molecular geometry, providing the ability to increase the yield of photoisomerization reactions. As a test case, we study the asymmetric proton transfer reaction in the electronically excited state of 3-aminoacrolein. Our results, which are robust for a range of realistic cavity parameters, highlight the advantages of hybrid cavities in cavity-induced photochemical processes.

I. INTRODUCTION

The coupling of organic molecules to confined light in a cavity and the formation of hybrid light–matter states, known as polaritons, enable the manipulation of both light and matter. In the past decade, their potential to tailor chemical reactions,[1–6] energy transport,[7–9] lasing,[10–12] and photon non-linearities[13] has been extensively studied. However, conventional photonic cavities, such as Fabry–Pérot resonators,[14] primarily enable collective light–matter coupling involving many molecules.[15] This delocalized coupling limits their ability to influence properties at the level of individual molecules.[16,17] In contrast, plasmonic nanocavities overcome this limitation by providing extreme sub-wavelength confinement, enabling significant single-molecule coupling strengths, and offering a promising platform for controlling individual molecular properties.[18–25]

Recently, several studies[26–29] have shown that the coupling of a molecular electronic excitation to a plasmonic mode, which features high loss due to metal absorption, can tailor molecular photorelaxation and, thus, affect the molecular structure and dynamics. This phenomenon is attributed to the Purcell effect,[30–34] wherein the cavity accelerates the molecular spontaneous emission rate by facilitating higher coupling to the free-space electromagnetic environment, as determined by the loss rate of the cavity. Thus, the Purcell effect, leveraging the high loss of the plasmonic mode, does not require the system to be in the strong coupling regime, where the light–matter coupling strength matches or exceeds the individual relaxation rates of the cavity and molecular excitation, but occurs

in the weak coupling regime. This makes Purcell-induced reactions more feasible for experimental realization.

In contrast to many previous studies that have focused on one-mode plasmonic cavities,[26–29] here we investigate the effect of a hybrid metallodielectric cavity, which involves both plasmonic and photonic modes. These (at least) two-mode cavities have gained significant theoretical[35–39] and experimental[40–43] interest in recent years, as they combine the low-loss properties of photonic microcavities with the highly localized fields of plasmonic modes, enabling novel functionalities. In this work, we explore their impact on the Purcell-induced photoisomerization reaction. In general, photoisomerization[44] is a process in which a molecule absorbs light, promoting it to an excited electronic state, followed by isomerization to a different geometric configuration, and a subsequent relaxation back to the ground state. Such a relaxation can either happen via conical intersection on the sub-picosecond timescale[45] or via spontaneous decay on a nanosecond timescale.[44] However, the spontaneous emission rate can be significantly accelerated via the Purcell effect by coupling the electronic transition to the cavity modes. Moreover, by selectively enhancing the decay rate to favor one geometry over another, the yield of the photoisomerization reaction can be increased. This selectivity is achieved through the energy selectivity of the cavity.

We propose that hybrid cavities provide a more energy-selective Purcell effect than single-mode cavities, enhancing the geometric selectivity of relaxation from the excited state and increasing the yield of photoisomerization reactions. As an illustrative case study, we investigate 3-aminoacrolein,[46] a model system for asymmetric proton transfer reactions in an excited electronic state. This model reaction, which demands high energy selectivity, highlights the advantages of hybrid cavities in controlling photoisomerization at the single-molecule level. The remainder of this paper is organized as follows: In Sec. II, we present the theoretical foundation of our work, explaining why hybrid cavities offer enhanced energy selectivity and detailing how the photoisomerization reaction can be theoretically studied, including an expression for the rate constant of cavity-mediated population transfer. Section III introduces the molecular case study, describing the computational methodology and the selected cavity parameters. In Sec. IV, we present the results that demonstrate the impact of the hybrid cavity on photoisomerization dynamics. Finally, in Sec. V, we summarize our findings.

II. THEORY

A. Multimode Purcell enhancement

The Purcell enhancement is determined in the weak coupling regime by the spectral density of the electromagnetic modes of the cavity, $J(\omega)$, at the transition frequency ω, where a higher spectral density corresponds to a stronger interaction with the cavity and, thus, a faster relaxation.[47] The energy gap between the electronic excited state and the electronic ground state dictates the transition frequency of the molecular excitation, given by $V_e(X) - V_g(X)$, where $V_g(X)$ and $V_e(X)$ are the potential energy surfaces of the ground and excited states as a function of the reaction coordinate X. Thus, when $J(\omega)$ varies strongly with ω, it provides a high selectivity in the spectral domain, which allows the possibility of selective coupling to certain regions on the potential energy surfaces, e.g., a specific molecular geometry. As a result, Purcell enhancement can favor specific relaxation pathways, thus influencing isomerization dynamics.

Achieving both strong Purcell enhancement and energy selectivity in single-mode cavities can be challenging. The spectral density of a single cavity mode can be characterized by a Lorentzian function,[48,49]

$$\mathrm{J}_{1\,\mathrm{mode}}(\omega) = \frac{g^2\kappa}{2\pi[(\omega_c-\omega)^2+\kappa^2/4]}, \tag{1}$$

where the linewidth κ represents the decay rate of the cavity mode. Here, ω_c is the frequency of the cavity mode, and g is its coupling strength to the molecule. Typically, a larger g is associated with a larger κ,[19–22] implying that a higher Purcell enhancement comes at the cost of broader spectral density, which reduces selectivity. Furthermore, the molecular enhanced decay is limited to half the cavity's loss rate, $\kappa/2$, emphasizing the importance of a high κ for achieving strong Purcell enhancement.[50]

Consequently, we propose using a hybrid metallodielectric cavity setup, sketched in Fig. 1, which combines two electromagnetic modes: one plasmonic and one photonic, to achieve both high Purcell enhancement and energy selectivity. The plasmonic mode provides significant coupling to the molecule, while selectivity is achieved through interference between the two modes. The spectral density of this hybrid cavity can be described as[49]

$$\mathrm{J}_{2\,\mathrm{mode}}(\omega) = \frac{1}{\pi}\mathrm{Im}\left\{\vec{g}^{\,T}\frac{1}{\mathbf{H}_{2\,\mathrm{mode}}-\omega}\vec{g}\right\}, \tag{2}$$

where $\vec{g} = \{g_1, g_2\}$ and

$$\mathbf{H}_{2\,\mathrm{mode}} = \begin{pmatrix} \omega_1 - \frac{i}{2}\kappa_1 & d \\ d & \omega_2 - \frac{i}{2}\kappa_2 \end{pmatrix}. \tag{3}$$

Here, ω_1 and ω_2 are the frequencies of the photonic and plasmonic modes, respectively; κ_1 and κ_2 are their decay rates; g_1 and g_2 represent their coupling strengths to the molecule; and d is the coupling between the two modes originating from the interaction between the electric field of the photonic mode and the plasmonic dipole moment. For $d = 0$, the spectral density reduces to the sum of two Lorentzians. However, for non-zero d, asymmetric lineshapes emerge. In the regime relevant to hybrid cavities, where the coupling strength and decay rate of the photonic mode are significantly smaller than those of the plasmonic mode,[51] that is, $\kappa_2 \gg \kappa_1$ and $g_2 \gg g_1$, the spectral density features two asymmetric peaks

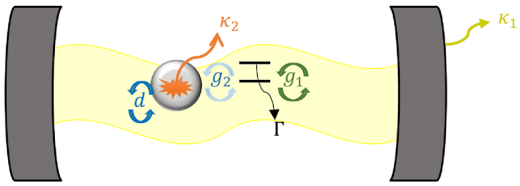

FIG. 1. Scheme of the hybrid metallodielectric cavity setup combining a Fabry–Pérot photonic mode with a plasmonic mode and interacting with a matter excitation described by a two-level system.

with the same amplitudes but different widths and a dip between them. In particular, when $g_1 = 0$ and $\kappa_1 = 0$, the spectral density simplifies to

$$J_{2\,\mathrm{mode}}(\omega) = \frac{g_2^2\kappa_2}{2\pi\left[\left(\omega_2 - \frac{d^2}{\omega_1-\omega} - \omega\right)^2 + \frac{\kappa_2^2}{4}\right]} \tag{4}$$

for $\omega \neq \omega_1$, featuring two maxima when $\omega_2 - \frac{d^2}{\omega_1-\omega} - \omega = 0$, and is zero at $\omega = \omega_1$. By selecting appropriate values for ω_1, ω_2, κ_2, g_2, and d, we engineer one of the spectral density peaks to be very narrow, allowing for highly energy-selective Purcell enhancement at the right frequency.

B. The rate constant for cavity-mediated population transfer

We study the Purcell-induced photoisomerization reaction by solving a set of rate equations that describe the population transfer between different vibrational states, representing different molecular isomers, in the molecular electronic ground state. These states are given by the eigenfunctions $|\Phi_n\rangle$ of $\hat{H}_g = \hat{T} + V_g(X)$, the nuclear Hamiltonian in the electronic ground state within the Born–Oppenheimer approximation, where $\hat{T}$ is the kinetic energy operator along the reaction coordinate X. The transfer of population from $|\Phi_i\rangle$ to $|\Phi_f\rangle$, mediated by excitation to the electronic excited state and decay through cavity losses, is a second-order process. Therefore, its rate constant $k_{i\to f}^{ESPT}$ is given by the Kramers–Heisenberg formula.[52] We use its non-Hermitian (NH) form[53–55] in order to account for cavity losses and the spontaneous decay rate of the molecule, Γ.

The hybrid cavity coupled to a molecular electronic excitation corresponds to the following NH Hamiltonian:

$$\hat{H}_0 = \hat{H}_g + \left(\hat{H}_e - \hat{H}_g - i\frac{\Gamma}{2}\right)\sigma_+\sigma_- + \sum_{n=1,2}\Big[\tilde{\omega}_n a_n^\dagger a_n + g_n D(X)(\sigma_+ a_n + a_n^\dagger \sigma_-)\Big] + d(a_1^\dagger a_2 + a_2^\dagger a_1), \tag{5}$$

where the rotating-wave approximation is applied. This Hamiltonian is the effective NH Hamiltonian[56] arising from the Lindblad master equation,[47,57] which is commonly used to describe lossy systems. Here, σ_- (σ_+) and a_n ($a_n^\dagger$) denote the annihilation (creation) operators of the molecular exciton and the two optical modes, respectively; $\hat{H}_e = \hat{T} + V_e(X)$ is the nuclear Hamiltonian in the excited electronic state; $\tilde{\omega}_n = \omega_n - i\frac{\kappa_n}{2}$ are the complex energies of the cavity modes; and $D(X)$ is the geometry-dependent transition dipole moment between the ground and the excited electronic states. The initial and final states of the population transfer correspond to the eigenstates of the zeroth optical excitation of $\hat{H}_0$. In these states, the cavity modes are in their corresponding vacuum state $|0\rangle$. They are given by $|i\rangle = |\Phi_i\rangle \otimes |0\rangle = |\Phi_i, 0\rangle$ and $|f\rangle = |\Phi_f\rangle \otimes |0\rangle = |\Phi_f, 0\rangle$ with the eigenenergies E_i and E_f. However, the states that mediate population transfer correspond to the first optical excitation manifold of $\hat{H}_0$ and are hybrid light–matter states, which we here will denote generically as polaritons without distinguishing between weak and strong coupling regimes. While the zeroth optical excitation of $\hat{H}_0$ is described by a Hermitian Hamiltonian, its first optically excited manifold is given by an NH Hamiltonian due to the difference in decay rate between the cavity modes (κ_1, κ_2) and the emitter (Γ). Therefore, to emphasize their different inner products,[58] the notation $|r)$ and $(r|$ is used, rather than $|r\rangle$ and $\langle r|$, for the right and left eigenstates of the first optical excitation manifold of $\hat{H}_0$. Since $\hat{H}_0$ is complex symmetric, $|r)$ is the same as $|r\rangle$, while $(r|$ is the complex conjugate of $\langle r|$. Moreover, these eigenstates are associated with complex eigenvalues $\tilde{E}_r$.[58]

The rate constant $k_{i\to f}^{ESPT}$ for the population transfer mediated by laser excitation and subsequent decay is then given by

$$k_{i\to f}^{ESPT} = \sum_k \left| \sum_r \frac{\langle 0, \Phi_f | \hat{V}_d^{(k)} | r)(r| \Omega D(X) \sigma_+ | \Phi_i, 0\rangle}{\tilde{E}_r - E_i - \hbar\omega_L} \right|^2, \tag{6}$$

where the index k sums over all possible decay channels. The matrix element $(r|\Omega D(X)\sigma_+|\Phi_i, 0\rangle$ describes the laser excitation of the initial state into the first optical excitation manifold of $\hat{H}_0$ through the molecular transition dipole $D(x)$ where Ω is the laser's field strength, and the denominator of Eq. (6), which does not diverge due to the complex value of $\tilde{E}_r$, describes the energy match with the laser frequency, ω_L. In addition, the matrix element $\langle 0, \Phi_f | \hat{V}_d^{(k)} | r)$ describes the subsequent relaxation from the optically excited manifold to the final state through the channel k. Following Refs. 53–55, we use $\sqrt{\Gamma}\sigma_-$ for the spontaneous emission of the molecule, and $\sqrt{\kappa_1}a_1$ and $\sqrt{\kappa_2}a_2$ for the two cavity losses as decay operators $\hat{V}_d^{(k)}$. The derivation of Eq. (6) with these decay operators from the Lindblad master equation using perturbation theory is presented in the Appendix.

In Eq. (6), two roles for the cavity setup are taken into account. First, the decay rate from the optically excited manifold to the electronic ground state is enhanced by opening additional decay channels beyond molecular spontaneous emission. Second, the eigenstates in the optically excited manifold of $\hat{H}_0$ are modified due to the formation of polaritons. If these polaritonic effects are neglected, the rate constant simplifies to

$$k_{i\to f}^{ESPT(nonP)} = \left| \sum_e \frac{\sqrt{\gamma_{ef}}\langle \Phi_f | D(X) | \phi_e\rangle\langle \phi_e | \Omega D(X) | \Phi_i\rangle}{E_e - i\Gamma/2 - E_i - \hbar\omega_L} \right|^2. \tag{7}$$

Here, we assume that only the eigenstates of $\hat{H}_e$, $|\phi_e\rangle$, with eigenvalues E_e, and not the polaritons $|r)$, which are the eigenstates of the first optical excitation manifold of $\hat{H}_0$, mediate the population transfer. In this case, the effect of the cavity setup on the decay to the electronic ground state is implicit and treated perturbatively,[47] assuming that the cavity setup can be described as a Markovian bath weakly coupled to the molecular excitation. As a result, the cavity-enhanced decay from $|\phi_e\rangle$ to $|\Phi_f\rangle$ is given by the matrix element $\langle \Phi_f | D(X) | \phi_e\rangle$ of the molecular transition dipole through which the cavity is coupled, multiplied by the square root of the rate $\gamma_{ef} = 2\pi J(E_e - E_f)$, where $J(\omega)$ is the spectral density of the cavity setup. When valid, Eq. (7) allows the calculation of cavity-mediated population transfer without explicitly considering the cavity degrees of freedom, simplifying the treatment of multiple modes. The laser excitation in Eq. (7) is treated similarly to Eq. (6), using the molecular transition dipole. The molecular spontaneous decay rate Γ is used to broaden the electronic excited states, preventing divergence of Eq. (7).

C. The molecular steady state

Our description of the dynamics of the cavity molecular system is based on coupled rate equations. To determine the rate constants $k_{i\to f}^{ESPT}$, we assign the rate equation to each vibrational state in the molecular electronic ground state,

$$\frac{dP_n(t)}{dt} = \sum_{m\neq n} k_{m\to n}^{tot} P_m(t) - P_n(t) \sum_{m\neq n} k_{n\to m}^{tot}, \tag{8}$$

where $P_n(t)$ is the population in the state Φ_n, and $k_{m\to n}^{tot}$ is the total rate constant for population transfer from the state Φ_m to state Φ_n, summing the rate constant $k_{m\to n}^{ESPT}$ derived above with the vibrational relaxation rate constant $k_{m\to n}^{VR}$. The last accounts for the effect of the nuclear degrees of freedom neglected when computing $k_{m\to n}^{ESPT}$ considering the reduced reaction coordinate and is given by

$$k_{m\to n}^{VR} = \gamma_0 |\langle \Phi_n | X | \Phi_m \rangle|^2 \tag{9}$$

for $E_m > E_n$, while it is zero for $E_m < E_n$. The matrix element $\langle \Phi_n | X | \Phi_m \rangle$ describes the transition dipole between the two states and $\gamma_0 = \frac{1}{ps}$. We find the photostationary state of this setup by locating the populations $P_n(t \to \infty)$ for which $\frac{dP_n(t\to\infty)}{dt} = 0$ for some n and which obey $\sum_n P_n(t \to \infty) = 1$. By determining which state is associated with each isomer of the molecule, the photoisomerization process can be studied.

III. THE MOLECULAR CASE STUDY

As a case study, we consider the asymmetric proton transfer reaction between the nitrogen atom and the oxygen atom in the second electronic excited state S_2 of (Z)-3-aminoacrylaldehyde.[46] The chosen molecular model represents an asymmetric variant of the well-studied symmetric proton transfer in (Z)-malondialdehyde.[59–61] The reaction of (Z)-3-aminoacrylaldehyde can be well approximated in a lower-dimensional subspace.[61–63] Both minimum structures (depicted in Fig. 2) and the transition state of the proton transfer reaction and the corresponding intrinsic reaction coordinate (IRC) were calculated in the electronic ground state S_0 at the ωB97XD/aug-CC-PVDZ[64,65] level of theory using the Gaussian 16 Rev.C.01 program package.[66] The potential energy curves for the optically accessible S_2 state and the corresponding transition dipole moment are obtained using linear-response time-dependent density functional theory within the Tamm–Dancoff approximation[67] with ten roots. All electronic structure calculations were performed in a reproducible environment using the Nix package manager together with NixOS-QChem[68] (commit f803c222) and Nixpkgs (nixpkgs, 23.05, commit 5550a85a). The last point of the IRC in both directions and the corresponding minima were used to extrapolate the potential energy curve to obtain a bound potential for S_2 and S_0. These potentials are plotted in the lower panel of Fig. 2 as a function of the reaction coordinate X defined by the IRC, which describes the proton transfer reaction between nitrogen and oxygen atoms. The kinetic energy operator along the reaction coordinate X is constructed within the G-matrix formalism,[69–71] as described in Ref. 72. It reads

$$\hat{T} \approx -\frac{\hbar^2}{2} \frac{\partial}{\partial X} G(X) \frac{\partial}{\partial X} \tag{10}$$

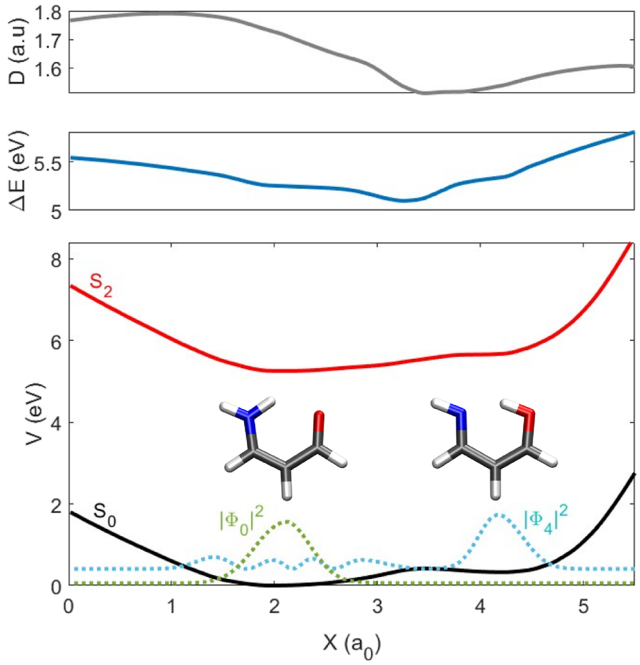

FIG. 2. Lower panel—the potential energy curves of the electronic ground (S_0) and second excited (S_2) states of (Z)-3-aminoacrylaldehyde as a function of the proton transfer reaction coordinate X defined by the IRC (see the main text). The vibrational wavefunctions associated with the ground state of each isomer are also plotted. Middle and upper panels—the excitation energy and the transition dipole between these two electronic states as a function of X.

with the G-matrix element $G(X)$ being computed via finite differences by displacement of the Cartesian molecular geometry along the internal coordinate. The vibrational states for the electronic ground state (S_0) and the excited state (S_2) along X, corresponding to the eigenstates of $\hat{H}_g$ and $\hat{H}_e$ [in Eq. (5)], were determined using the discrete variable representation (DVR) method and the one-dimensional particle-in-a-box basis functions. The chosen parameters, for which we obtain converged results, are as follows: box length $L = 6$ a.u., and the number of basis functions $n = 100$. The vibrational ground state in S_0, $\Phi_0(X)$, presented in the lower panel of Fig. 2, is localized in the left well. After the molecule has been excited to the second excited electronic state, the excited-state wave packet can propagate between the left and right wells of the S_2 potential curve. The subsequent decay back to the ground electronic state S_0 can give rise to the product of the proton transfer reaction as the right well in the S_0 potential curve is populated. In particular, we are interested in transferring the population to the fourth vibrational state in S_0, $\Phi_4(X)$, which is localized mostly in the right well, as is also shown in the lower panel of Fig. 2.

The enhancement of population transfer to $\Phi_4(X)$ by coupling the molecular excitation $S_0 \to S_2$ to a cavity setup requires high energy selectivity, since both the excitation energy, given by the difference between the two potentials $\Delta E(X) = V_{S_2}(X) - V_{S_0}(X)$ (middle panel of Fig. 2), and the electronic transition dipole $D(X)$ (upper panel of Fig. 2), are similar between the two nuclear configurations.

TABLE I. Optimization of the cavities' parameters to achieve the highest steady-state population in $\Phi_4(X)$ for the intracavity laser strength $\Omega = 10^{-5}$. The optimal values for the two-mode cavity are given in the first column, and for the one-mode cavity, they are given in the second column.

	Two-mode optimal (eV)	One-mode optimal (eV)
ω_1	5.351	⋯
ω_2	6.816	5.276
κ_2	0.335	0.448
g_2	0.046	0.019
d	0.164	⋯

Thus, it fits the purpose of demonstrating the benefits of the hybrid metallodielectric cavity in enhancing photoisomerization reactions. The laser frequency used matches the highest Franck–Condon factor corresponding to $\omega_L = E_{0,e} - E_{0,g} = 5.254$ eV, where $E_{0,e/g}$ are the lowest vibrational eigenvalues of the two electronic states. In addition, we consider $\Gamma = 10^{-7}$ a.u. = 4 ns^{-1} as the rate of spontaneous decay of the molecule. For simplicity, we set the coupling strength and decay rate of the photonic mode to $g_1 = 0$ and $\kappa_1 = 0$. The robustness of the results over a wide range of physically relevant values for g_1 and κ_1 is demonstrated in Fig. 7. The other parameters of the hybrid cavity, $\omega_1, \omega_2, \kappa_2, g_2$, and d, are chosen using the constrained nonlinear optimization algorithm of MATLAB R2024a by looking for a maximum value of P_4 where $\Omega = 10^{-5}$ a.u. = $5.142 \frac{\text{V}}{\mu m}$. It is important to note that the intracavity electric field for a given incoming laser field is enhanced relative to free space.[73] To compensate for this and focus solely on the cavity's effect in accelerating and tailoring the spontaneous emission relevant to the photoisomerization reaction, we parameterize the system in terms of the effective intracavity electric field strength Ω that the molecule feels, instead of the original free-space laser field strength. The optimized values are summarized in Table I and are feasible in accordance with the existing literature. Although we keep the plasmonic coupling strength g_2 within the weak coupling regime and up to 100 meV as realized in Refs. 19–22, the coupling between the modes d can be strong.[74] In addition, a high plasmonic decay rate equivalent to 0.5 eV was calculated for an aluminum sphere.[28] For comparison, we also optimize the results for a one-mode cavity, whose only parameters are ω_2, κ_2, and g_2, and their optimized values are given in the second column of Table I.

IV. RESULTS AND DISCUSSION

The steady-state population of $\Phi_4(X)$, P_4, is presented in Fig. 3 as a function of the intracavity laser strength Ω for both the optimized hybrid (two-mode) and one-mode cavity setups. For comparison, we also show the case without any cavity coupling, where the spontaneous emission of the molecule solely governs the decay from the electronically excited state. The dependence of P_4 on Ω reflects the interplay between the timescales of population transfer via the electronic excited state and the vibrational relaxation. The latter is fixed at 1 picosecond in our calculations and remains independent of Ω. For very small Ω, vibrational relaxation dominates the dynamics, leading to a localization of the population in the vibronic ground state, with $P_4 \to 0$. As Ω increases, the transfer

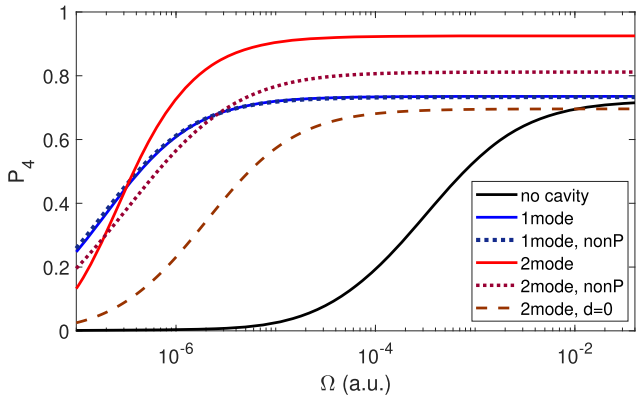

FIG. 3. Photo steady-state population of the vibrational state Φ_4 in the electronic ground state (S_0), P_4, as a function of the intracavity laser field strength Ω for a setup of no cavity, one-mode cavity, and two-mode cavity. The parameters of the cavities were optimized to achieve a high population when $\Omega = 10^{-5}$ a.u., as described in the main text. The results obtained when neglecting the coupling between the two modes d and when considering only the non-polaritonic effect of the two-mode cavity [Eq. (7)] are also presented.

of population via the electronic excited state becomes more significant, facilitating the population of $\Phi_4(X)$ and increasing P_4. For sufficiently large Ω, P_4 reaches a maximal constant value, indicating that the rate of population transfer through the electronic excited state exceeds the vibrational relaxation rate. Comparing the results of the one-mode cavity and the two-mode cavity with the cavity-free case shows that the cavities accelerate population transfer to $\Phi_4(X)$, as they enable maximal population at lower Ω values than in the cavity-free setup. This acceleration arises from the Purcell effect, which enhances the spontaneous emission from S_2 to S_0. However, while the one-mode cavity achieves a maximal value of P_4 of ~70%, similar to the cavity-free setup, the two-mode cavity increases this value to greater than 90%. This enhancement highlights the selective effect of the hybrid cavity, as analyzed through the spectral densities below.

The spectral densities for the one-mode and two-mode cavity setups, $J_{1\text{mode}}(\omega)$ and $J_{2\text{mode}}(\omega)$, are shown in Fig. 4 and are given by Eqs. (1) and (4), respectively. $J_{1\text{mode}}(\omega)$ exhibits a broad peak, whereas $J_{2\text{mode}}(\omega)$ features a narrower and asymmetric peak in the relevant frequency range for spontaneous emission from S_2 to S_0. This difference in peak linewidths indicates that the hybrid cavity offers a higher energy selectivity, which selectively enhances the decay from S_2 to $\Phi_4(X)$. In the Markovian and weak-coupling regime, where the population in cavity modes is negligible, the effect of the cavities can be treated perturbatively. Consequently, the Purcell-enhanced spontaneous decay rate depends on the value of the spectral density at the transition frequency, as taken into account in Eq. (7). We present in Fig. 3 in dotted lines the population P_4 obtained when replacing $k_{i\to f}^{ESPT}$ [Eq. (6)] with $k_{i\to f}^{ESPT(nonP)}$ [Eq. (7)] for the two cavity setups. For the one-mode cavity, whose coupling strength is smaller than that of the two-mode cavity, this approximate calculation reproduces the full calculation, while for the two-mode cavity, it does not, showing energy exchange between the molecule and cavity modes in the hybrid

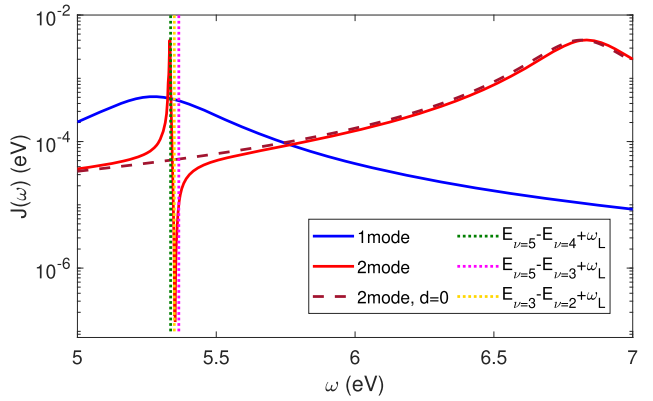

FIG. 4. Spectral densities of the one-mode and two-mode cavities corresponding to the results presented in Fig. 3. The vertical dashed lines indicate the energy gaps between different transitions and demonstrate the high selectivity achieved by the two-mode cavities.

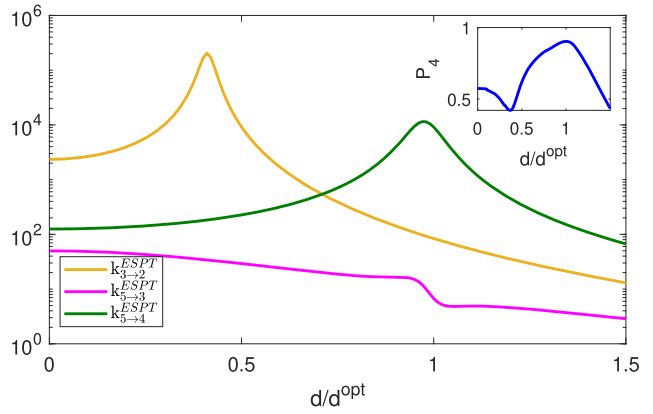

FIG. 5. Rate constants of competing transitions as a function of the coupling between the two modes d. The largest value for population P_4 is obtained for d^{opt}, as shown in the inset.

setup. Importantly, the approximate calculation still predicts higher P_4 for the two-mode cavity than for the one-mode cavity. This reveals a strong connection between the line shape of the spectral density and the enhancement of the population, strengthening the interpretation that the increased population transfer to $\Phi_4(X)$ in the hybrid cavity setup indeed stems from its superior energy selectivity.

The narrow peak of $J_{2\text{mode}}$, which results in the high energy selectivity of the hybrid cavity, arises from the interference between the two modes due to their non-zero coupling, d, as discussed in Sec. II. In Fig. 3, the results for the two-mode cavity with $d = 0$ are shown in a dashed line, where the corresponding spectral density is plotted in Fig. 4 (also in a dashed line). Since $g_1 = 0$, this spectral density fits that of a one-mode cavity characterized by the parameters of the plasmonic mode, which is far detuned from the molecular excitation energies (Fig. 4). Consequently, this spectral density remains approximately constant in the relevant energy range for spontaneous emission from S_2 to S_0, leading to an unselective acceleration of emission and no increase in the asymptote of P_4 compared to the cavity-free case (Fig. 3). To further investigate the role of d and to highlight the importance of energy selectivity of the hybrid cavity setup in the enhancement of excited-state mediated population transfer, we compare the rate constants of the competing transitions, $k^{ESPT}_{3\to2}$, $k^{ESPT}_{5\to3}$, and $k^{ESPT}_{5\to4}$, as functions of d in Fig. 5. The vertical dotted lines in Fig. 4 indicate the emission frequencies of these competing transitions, given by $E_i + \omega_L - E_f$, where E_i and E_f are the energies of the initial and final states, respectively, and ω_L is the laser frequency. Since these frequencies are very similar, the one-mode cavity and the setup for $d = 0$ enhance these transitions unselectively, leading to the second highest populated state being $\Phi_2(X)$ due to the transitions $5 \to 3 \to 2$. In contrast, the two-mode cavity selectively accelerates the transition $5 \to 4$ while suppressing the transitions $5 \to 3 \to 2$, thereby enhancing P_4 by carefully choosing d, ω_1, and ω_2 to tune the narrow peak's frequency [as determined from Eq. (4)]. This high energy selectivity is demonstrated in Fig. 5, which shows that varying d, and thus varying the frequency corresponding to the maximum of the narrow peak in $J_{2\text{mode}}$, results in different transitions being accelerated. Note that higher values of d correspond to lower frequencies for the narrow peak, which means that the maximal value of $k^{ESPT}_{3\to2}$ whose transition energy exceeds that of $k^{ESPT}_{5\to4}$ is obtained at smaller values of d.

According to Eq. (4), the parameters d, ω_L, ω_1, and ω_2 determine the position of the maximum of $J_{2\text{mode}}(\omega)$ and are, therefore, responsible for achieving the required energy selectivity for population transfer to $\Phi_4(X)$. This is demonstrated in Fig. 5 for variation in d. In contrast, the parameters g_2 and κ_2 dictate the amplitude of $J_{2\text{mode}}(\omega)$. In particular, $J_{2\text{mode}}(\omega)$ scales linearly with g_2 for all ω, while its scaling with κ_2 is inversely proportional when $|\omega_2 - \frac{d^2}{\omega_1 - \omega} - \omega| \ll \kappa_2/2$ and linear when $|\omega_2 - \frac{d^2}{\omega_1 - \omega} - \omega| \gg \kappa_2/2$. In Fig. 6, we present the minimal intracavity laser field strength Ω_{min} required for $P_4 > 0.9$ as a function of g_2 when $\kappa_2 = \kappa_2^{\text{opt}}$ by the purple line and as a function of κ_2 when $g_2 = g_2^{\text{opt}}$ by the light green line. The parameters g_2^{opt} and κ_2^{opt} were optimized to achieve the largest value for P_4 for the two-mode cavity setup and are given in Table I. Although the maximum value of P_4 remains relatively insensitive to variations in g_2 or in κ_2, it varies with Ω_{min}, i.e., the minimum laser power required to ensure that population transfer via the electronic excited state overcomes vibrational relaxation. For a low amplitude of $J_{2\text{mode}}(\omega)$, the acceleration of spontaneous emission by the cavity is weaker, necessitating a stronger laser to achieve maximal P_4. However, if the amplitudes become too high, the spectral density description of the cavity-enhanced decay rate becomes invalid. Thus, Fig. 6 indicates that there exists an optimal range for g_2 and κ_2 where population transfer via the excited state occurs most rapidly.

Finally, we discuss the effects of the photonic mode's parameters. While its coupling strength g_1 and its decay rate κ_1 are both set to 0 in Figs. 3–6, we present P_4 in Fig. 7 as a function of κ_1 and g_1 for $\Omega = 10^{-5}$ a.u. As shown, the enhanced energy transfer in the hybrid cavity remains robust across a wide range of κ_1 and g_1. Only when g_1 reaches $g_2^{\text{opt}}/10$ and κ_1 reaches $\kappa_2^{\text{opt}}/100$, the enhancement of population transfer to $\Phi_4(X)$ in the two-mode

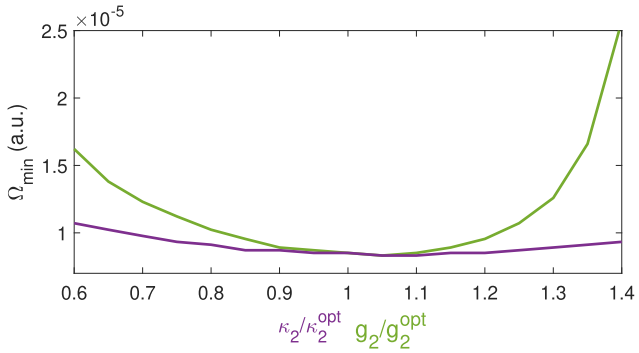

FIG. 6. Minimal intracavity laser field strength Ω_{min} for which $P_4 > 0.9$ as a function of the plasmonic decay rate κ_2 and as a function of the plasmonic coupling strength g_2.

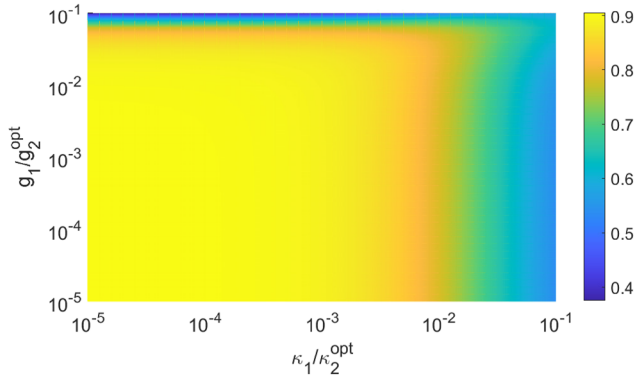

FIG. 7. P_4 as a function of g_1 and κ_1, the coupling strength between the photonic mode and the molecular electronic excitation and the photonic decay rate, respectively.

cavity is lost. In these regimes, the interference between the photonic and plasmonic modes weakens, leading to a broader peak and reduced energy selectivity. It is important to note that in realistic Fabry–Pérot cavities, additional modes beyond the one explicitly included in our model can also be present, potentially introducing decay channels that reduce energy selectivity. However, isolating a photonic mode within a few electronvolts is experimentally feasible, as demonstrated in Refs. 75 and 76. Furthermore, even if additional modes appear within the 4–6 eV range relevant to the vibronic transitions in our case study, their impact can be mitigated by ensuring they are not resonant with the molecule's vibronic transitions, thus preventing the opening of unwanted decay channels. These effects can be further reduced by optimizing the cavity mode parameters, as shown in Table I.

V. SUMMARY

We have explored how hybrid metallodielectric cavities can control photoisomerization reactions at the single-molecule level. These reactions can be tailored via the cavity-induced Purcell effect, which enhances relaxation from the electronically excited state to the desired geometry. In contrast to previous works,[26–29] which studied this effect in one-mode plasmonic cavities, we demonstrate that interference between two modes in a hybrid cavity plays a crucial role in achieving energy-selective Purcell enhancement. This selectivity leads to higher photoisomerization yields compared to those of one-mode cavities or cavity-free setups. To illustrate this, we have examined the excited-state asymmetric proton transfer in (Z)-3-aminoacrylaldehyde. Based on electronic-structure calculations and using rate equations that incorporate cavity effects, we study population transfer from the vibronic ground state (proton located on the nitrogen atom) to the fourth excited vibrational state (proton located on the oxygen atom). Optimized, yet realistic, parameters for one-mode plasmonic and two-mode hybrid cavities were used. Our results reveal that while both cavity setups accelerate the proton transfer reaction and reduce the required laser intensity, the hybrid cavity achieves a significantly higher population transfer. This enhancement comes from the superior energy selectivity of the hybrid cavity, which only targets the desired relaxation pathway. We have also analyzed the sensitivity of these results against variations in the parameters of the hybrid cavity and found that it is quite robust. These findings highlight the potential of hybrid cavities for controlling photochemical reactions, paving the way for future applications in cavity-induced chemistry.

ACKNOWLEDGMENTS

This project has received the funding from the European Research Council (ERC) under the European Union's Horizon 2020 research and innovation program (Grant Agreement No. 852286). The support from the Swedish Research Council (Grant No. VR 2022-05005) is acknowledged. In addition, this project received the funding from the European Union's Horizon 2020 research and innovation program through Agreement No. 101070700 (MIRAQLS), as well as under the Marie Skłodowska-Curie Grant Agreement No. 101034324. Furthermore, this work was funded by the Spanish Ministry of Science, Innovation, and Universities-Agencia Estatal de Investigación through Grant Nos. PID2021-125894NB-I00, EUR2023-143478, and CEX2023-001316-M (through the María de Maeztu program for Units of Excellence in R & D).

AUTHOR DECLARATIONS

Conflict of Interest

The authors have no conflicts to disclose.

Author Contributions

Anael Ben-Asher: Conceptualization (equal); Data curation (lead); Funding acquisition (lead); Investigation (lead); Writing – original draft (lead); Writing – review & editing (equal). **Thomas Schnappinger**: Conceptualization (equal); Data curation (equal); Investigation (equal); Writing – original draft (equal); Writing – review & editing (equal). **Markus Kowalewski**: Conceptualization (equal); Funding acquisition (lead); Project administration (lead); Supervision (equal); Writing – original draft (supporting); Writing – review

& editing (equal). **Johannes Feist**: Conceptualization (equal); Funding acquisition (lead); Project administration (lead); Supervision (equal); Writing – original draft (supporting); Writing – review & editing (equal).

DATA AVAILABILITY

The data that support the findings of this study are available from the corresponding author upon reasonable request.

APPENDIX: DERIVATION OF THE RATE CONSTANT $k_{i\to f}^{ESPT}$ FROM THE LINDBLAD MASTER EQUATION

Here, we derive Eq. (6) from the Lindblad master equation associated with $\hat{H}_0$, treating perturbatively the interaction with the laser and the population transfer to the electronic ground state. This derivation naturally yields the decay operators for the spontaneous emission of the molecule and the cavity losses, in agreement with Refs. 53–55.

The Lindblad master equation associated with the effective NH Hamiltonian $\hat{H}_0$ [Eq. (5)] that also considers the driving by the laser, $\hat{V}_L(t) = \Omega D(X)(e^{-i\omega_L t}\sigma_+ + e^{+i\omega_L t}\sigma_-)$, can be written as

$$\frac{d\rho(t)}{dt} = -\frac{i}{\hbar}\left[\hat{H}(t)\rho(t) - \rho(t)\hat{H}^\dagger(t)\right] + \sum_k \hat{V}_d^{(k)}\rho(t)\hat{V}_d^{(k)\dagger}, \quad \text{(A1)}$$

where $\hat{H}(t) = \hat{H}_0 + \hat{V}_L(t)$ and the sum over k includes the jump operators of the Lindblad superoperator corresponding to the cavity losses and the spontaneous emission of the molecule, such that $\hat{V}_d^{(1)} = \sqrt{\kappa}\sigma_-$, $\hat{V}_d^{(2)} = \sqrt{\kappa_1}a_1$, and $\hat{V}_d^{(3)} = \sqrt{\kappa_2}a_2$.

We consider the eigenstates of $\hat{H}_0$ and $\hat{H}_0^\dagger$, given by $\hat{H}_0|n) = \tilde{E}_n|n)$ and $\hat{H}_0^\dagger|n^*) = \tilde{E}_n^*|n^*)$, respectively, as the non-perturbative zeroth-order states where the notation $|\ldots)$ and $(\ldots|$ rather than $|\ldots\rangle$ and $\langle\ldots|$ is used for the right and left eigenstates of NH Hamiltonians, and $\tilde{E}_n$ is complex. Because $\hat{H}_0$ and $\hat{H}_0^\dagger$ are the complex symmetric Hamiltonians, the eigenstates $|n^*)$ and $(n^*|$ are the complex conjugates of $|n)$ and $(n|$, respectively. Furthermore, the states in the zeroth optical excitation manifold of $\hat{H}_0$ and $\hat{H}_0^\dagger$, which can be described by a Hermitian Hamiltonian, obey $|n^*) = |n) = |n\rangle$ and $(n^*| = (n| = \langle n|$ and are real. We express the density matrix $\rho(t)$ in terms of these zeroth-order states as $\rho(t) = \sum_{m,n} b_{mn}(t)|m)(n^*|$, and obtain the master equation for the coefficient $b_{mn} = (m|\rho(t)|n^*)$,

$$\begin{aligned}\frac{db_{mn}(t)}{dt} = &-\frac{i}{\hbar}\Big((\tilde{E}_m - \tilde{E}_n^*)b_{mn}(t) \\ &+ \sum_l (m|\hat{V}_L(t)|l)b_{ln}(t) + \sum_p (p^*|\hat{V}_L(t)|n^*)b_{mp}(t)\Big) \\ &+ \sum_k\sum_{l,p}(m|\hat{V}_d^{(k)}|l)(p^*|\hat{V}_d^{(k)\dagger}|n^*)b_{lp}(t). \quad \text{(A2)}\end{aligned}$$

Next, we isolate the effect of the laser interaction and Lindblad jump operators by transforming Eq. (A2) to the NH interaction picture, as in Ref. 77. This yields the following master equation:

$$\begin{aligned}\frac{d\tilde{b}_{mn}(t)}{dt} = &-\frac{i}{\hbar}\Bigg(\sum_l (m|\hat{V}_L(t)|l)e^{i(\tilde{E}_m-\tilde{E}_l)t/\hbar}\tilde{b}_{ln}(t) \\ &+ \sum_p (p^*|\hat{V}_L(t)|n^*)e^{i(\tilde{E}_p^*-\tilde{E}_n^*)t/\hbar}\tilde{b}_{mp}(t)\Bigg) + \sum_k\sum_{l,p}\tilde{b}_{lp}(t) \\ &\times (m|\hat{V}_d^{(k)}|l)e^{i(\tilde{E}_m-\tilde{E}_l)t/\hbar}(p^*|\hat{V}_d^{(k)\dagger}|n^*)e^{i(\tilde{E}_p^*-\tilde{E}_n^*)t/\hbar}, \quad \text{(A3)}\end{aligned}$$

where the coefficients of the density matrix in the interaction picture are given by $\tilde{b}_{mn}(t) = e^{i(\tilde{E}_m-\tilde{E}_n^*)t/\hbar}b_{mn}(t)$. We treat Eq. (A3) perturbatively by iteratively solving it up to the second order with the initial condition $\tilde{b}_{mn}(0) = \delta_{im}\delta_{in}$. Note that $|i\rangle = |i) = |i^*)$ is the initial state of the population transfer process corresponding to the zeroth optical excitation of $\hat{H}_0$ and $\hat{H}_0^\dagger$. As a result, we obtain that the elements of the density matrix in the first optical excitation manifold of $\hat{H}_0$ and $\hat{H}_0^\dagger$ obey

$$\begin{aligned}\tilde{b}_{mn}(t) = &\frac{i}{\hbar}\Omega^2\,(i|D(X)\sigma_-|n^*)(m|D(x)\sigma_+|i\rangle \\ &\times\int_0^t dt'\Bigg(\frac{e^{i(\tilde{E}_m-\tilde{E}_n)t'/\hbar} - e^{i(\tilde{E}_m-E_i-\hbar\omega_L)t'/\hbar}}{E_i+\hbar\omega_L-\tilde{E}_n^*} \\ &+ \frac{e^{i(\tilde{E}_m-\tilde{E}_n)t'/\hbar} - e^{i(E_i+\hbar\omega_L-\tilde{E}_n^*)t'/\hbar}}{\tilde{E}_m-E_i-\hbar\omega_L}\Bigg), \quad \text{(A4)}\end{aligned}$$

where E_i is the energy of the initial state and is real.

Finally, we substitute Eq. (A4) into Eq. (A3) and neglect higher-order terms of Ω to obtain a master equation for the population in the final state $b_{ff}(t)$,

$$\begin{aligned}\frac{db_{ff}(t)}{dt} = &\Omega^2\sum_k\sum_{l,p}\frac{\langle i|D(X)\sigma_-|p^*)(p^*|\hat{V}_d^{(k)\dagger}|f\rangle}{E_i+\hbar\omega_L-\tilde{E}_p^*} \\ &\times\frac{\langle f|\hat{V}_d^{(k)}|l)(l|D(x)\sigma_+|i\rangle}{\tilde{E}_l-E_i-\hbar\omega_L}\Big(1+e^{i(\tilde{E}_p^*-\tilde{E}_l)t/\hbar} \\ &- e^{i(E_i+\hbar\omega_L-\tilde{E}_l)t/\hbar} - e^{i(\tilde{E}_p^*-E_i-\hbar\omega_L)t/\hbar}\Big). \quad \text{(A5)}\end{aligned}$$

Since $|f\rangle = |f) = |f^*)$ is a state within the zeroth optical excitation subspace of $\hat{H}_0$ and $\hat{H}_0^\dagger$, it is associated with the real eigenvalue E_f and $b_{ff}(t) = \tilde{b}_{ff}(t)$. As $t\to\infty$, the time-dependent exponents in Eq. (A5) vanish due to the positive imaginary part of $\tilde{E}_p^*$ and the negative imaginary part of $\tilde{E}_l$. Since $(l|D(x)\sigma_+|i\rangle = [\langle i|D(X)\sigma_-|k^*)]^*$ and $\langle f|\hat{V}_d^{(k)}|l) = [(l^*|\hat{V}_d^{(k)\dagger}|f\rangle]^*$, this results in the rate constant $k_{i\to f}^{ESPT} = \frac{db_{ff}(t\to\infty)}{dt}$ given in Eq. (6).

REFERENCES

[1] J. Feist, J. Galego, and F. J. Garcia-Vidal, "Polaritonic chemistry with organic molecules," ACS Photonics **5**, 205–216 (2018).
[2] M. Hertzog, M. Wang, J. Mony, and K. Börjesson, "Strong light–matter interactions: A new direction within chemistry," Chem. Soc. Rev. **48**, 937–961 (2019).
[3] F. Herrera and J. Owrutsky, "Molecular polaritons for controlling chemistry with quantum optics," J. Chem. Phys. **152**, 100902 (2020).

[4]T. W. Ebbesen, A. Rubio, and G. D. Scholes, "Introduction: Polaritonic chemistry," Chem. Rev. **123**, 12037–12038 (2023).
[5]R. Bhuyan, J. Mony, O. Kotov, G. W. Castellanos, J. Gómez Rivas, T. O. Shegai, and K. Börjesson, "The rise and current status of polaritonic photochemistry and photophysics," Chem. Rev. **123**, 10877–10919 (2023).
[6]M. Kowalewski, K. Bennett, and S. Mukamel, "Non-adiabatic dynamics of molecules in optical cavities," J. Chem. Phys. **144**, 054309 (2016).
[7]M. Balasubrahmaniyam, A. Simkhovich, A. Golombek, G. Sandik, G. Ankonina, and T. Schwartz, "From enhanced diffusion to ultrafast ballistic motion of hybrid light–matter excitations," Nat. Mater. **22**, 338–344 (2023).
[8]I. Sokolovskii, R. H. Tichauer, D. Morozov, J. Feist, and G. Groenhof, "Multi-scale molecular dynamics simulations of enhanced energy transfer in organic molecules under strong coupling," Nat. Commun. **14**, 6613 (2023).
[9]G. Sandik, J. Feist, F. J. García-Vidal, and T. Schwartz, "Cavity-enhanced energy transport in molecular systems," Nat. Mater. (published online 2024).
[10]J. Kasprzak, M. Richard, S. Kundermann, A. Baas, P. Jeambrun, J. M. J. Keeling, F. Marchetti, M. Szymańska, R. André, J. Staehli, *et al.*, "Bose–Einstein condensation of exciton polaritons," Nature **443**, 409–414 (2006).
[11]S. Kéna-Cohen and S. Forrest, "Room-temperature polariton lasing in an organic single-crystal microcavity," Nat. Photonics **4**, 371–375 (2010).
[12]K. B. Arnardottir, A. J. Moilanen, A. Strashko, P. Törmä, and J. Keeling, "Multimode organic polariton lasing," Phys. Rev. Lett. **125**, 233603 (2020).
[13]C. Toninelli, I. Gerhardt, A. Clark, A. Reserbat-Plantey, S. Götzinger, Z. Ristanović, M. Colautti, P. Lombardi, K. Major, I. Deperasińska, *et al.*, "Single organic molecules for photonic quantum technologies," Nat. Mater. **20**, 1615–1628 (2021).
[14]J. M. Gérard, D. Barrier, J. Marzin, R. Kuszelewicz, L. Manin, E. Costard, V. Thierry-Mieg, and T. Rivera, "Quantum boxes as active probes for photonic microstructures: The pillar microcavity case," Appl. Phys. Lett. **69**, 449–451 (1996).
[15]D. G. Lidzey, D. D. C. Bradley, T. Virgili, A. Armitage, M. S. Skolnick, and S. Walker, "Room temperature polariton emission from strongly coupled organic semiconductor microcavities," Phys. Rev. Lett. **82**, 3316 (1999).
[16]J. Galego, F. J. Garcia-Vidal, and J. Feist, "Cavity-induced modifications of molecular structure in the strong-coupling regime," Phys. Rev. X **5**, 041022 (2015).
[17]J. A. Ćwik, P. Kirton, S. De Liberato, and J. Keeling, "Excitonic spectral features in strongly coupled organic polaritons," Phys. Rev. A **93**, 033840 (2016).
[18]P. Törmä and W. L. Barnes, "Strong coupling between surface plasmon polaritons and emitters: A review," Rep. Prog. Phys. **78**, 013901 (2014).
[19]R. Chikkaraddy, B. De Nijs, F. Benz, S. J. Barrow, O. A. Scherman, E. Rosta, A. Demetriadou, P. Fox, O. Hess, and J. J. Baumberg, "Single-molecule strong coupling at room temperature in plasmonic nanocavities," Nature **535**, 127–130 (2016).
[20]Y. Zhang, Q.-S. Meng, L. Zhang, Y. Luo, Y.-J. Yu, B. Yang, Y. Zhang, R. Esteban, J. Aizpurua, Y. Luo, *et al.*, "Sub-nanometre control of the coherent interaction between a single molecule and a plasmonic nanocavity," Nat. Commun. **8**, 15225 (2017).
[21]N. Kongsuwan, A. Demetriadou, R. Chikkaraddy, F. Benz, V. A. Turek, U. F. Keyser, J. J. Baumberg, and O. Hess, "Suppressed quenching and strong-coupling of Purcell-enhanced single-molecule emission in plasmonic nanocavities," ACS Photonics **5**, 186–191 (2018).
[22]O. S. Ojambati, R. Chikkaraddy, W. D. Deacon, M. Horton, D. Kos, V. A. Turek, U. F. Keyser, and J. J. Baumberg, "Quantum electrodynamics at room temperature coupling a single vibrating molecule with a plasmonic nanocavity," Nat. Commun. **10**, 1049 (2019).
[23]J. J. Baumberg, J. Aizpurua, M. H. Mikkelsen, and D. R. Smith, "Extreme nanophotonics from ultrathin metallic gaps," Nat. Mater. **18**, 668–678 (2019).
[24]J. Heintz, N. Markešević, E. Y. Gayet, N. Bonod, and S. Bidault, "Few-molecule strong coupling with dimers of plasmonic nanoparticles assembled on DNA," ACS Nano **15**, 14732 (2021).
[25]J.-Y. Li, W. Li, J. Liu, J. Zhong, R. Liu, H. Chen, and X.-H. Wang, "Room-Temperature strong coupling between a single quantum dot and a single plasmonic nanoparticle," Nano Lett. **22**, 4686 (2022).
[26]S. Felicetti, J. Fregoni, T. Schnappinger, S. Reiter, R. de Vivie-Riedle, and J. Feist, "Photoprotecting uracil by coupling with lossy nanocavities," J. Phys. Chem. Letters **11**, 8810–8818 (2020).
[27]D. Wellnitz, S. Schütz, S. Whitlock, J. Schachenmayer, and G. Pupillo, "Collective dissipative molecule formation in a cavity," Phys. Rev. Lett. **125**, 193201 (2020).
[28]J. Torres-Sánchez and J. Feist, "Molecular photodissociation enabled by ultrafast plasmon decay," J. Chem. Phys. **154**, 014303 (2021).
[29]D. Wellnitz, G. Pupillo, and J. Schachenmayer, "A quantum optics approach to photoinduced electron transfer in cavities," J. Chem. Phys. **154**, 054104 (2021).
[30]E. M. Purcell, "Proceedings of the American physical society," Phys. Rev. **69**, 674 (1946).
[31]K. Drexhage, "Influence of a dielectric interface on fluorescence decay time," J. Lumin. **1–2**, 693–701 (1970).
[32]S. Kühn, U. Håkanson, L. Rogobete, and V. Sandoghdar, "Enhancement of single-molecule fluorescence using a gold nanoparticle as an optical nanoantenna," Phys. Rev. Lett. **97**, 017402 (2006).
[33]P. Anger, P. Bharadwaj, and L. Novotny, "Enhancement and quenching of single-molecule fluorescence," Phys. Rev. Lett. **96**, 113002 (2006).
[34]A. Kinkhabwala, Z. Yu, S. Fan, Y. Avlasevich, K. Müllen, and W. Moerner, "Large single-molecule fluorescence enhancements produced by a bowtie nanoantenna," Nat. Photonics **3**, 654–657 (2009).
[35]X. Yang, A. Ishikawa, X. Yin, and X. Zhang, "Hybrid Photonic–Plasmonic crystal nanocavities," ACS Nano **5**, 2831–2838 (2011).
[36]P. Peng, Y.-C. Liu, D. Xu, Q.-T. Cao, G. Lu, Q. Gong, Y.-F. Xiao, *et al.*, "Enhancing coherent light-matter interactions through microcavity-engineered plasmonic resonances," Phys. Rev. Lett. **119**, 233901 (2017).
[37]B. Gurlek, V. Sandoghdar, and D. Martín-Cano, "Manipulation of quenching in nanoantenna–emitter systems enabled by external detuned cavities: A path to enhance strong-coupling," ACS Photonics **5**, 456–461 (2018).
[38]N. Thakkar, M. T. Rea, K. C. Smith, K. D. Heylman, S. C. Quillin, K. A. Knapper, E. H. Horak, D. J. Masiello, and R. H. Goldsmith, "Sculpting fano resonances to control photonic–plasmonic hybridization," Nano Lett. **17**, 6927–6934 (2017).
[39]A. Ben-Asher, A. I. Fernández-Domínguez, and J. Feist, "Non-hermitian anharmonicity induces single-photon emission," Phys. Rev. Lett. **130**, 243601 (2023).
[40]M. Barth, S. Schietinger, S. Fischer, J. Becker, N. Nüsse, T. Aichele, B. Löchel, C. Sönnichsen, and O. Benson, "Nanoassembled plasmonic-photonic hybrid cavity for tailored light-matter coupling," Nano Lett. **10**, 891–895 (2010).
[41]Y. Luo, M. Chamanzar, A. Apuzzo, R. Salas-Montiel, K. N. Nguyen, S. Blaize, and A. Adibi, "On-chip hybrid photonic–plasmonic light concentrator for nanofocusing in an integrated silicon photonics platform," Nano Lett. **15**, 849–856 (2015).
[42]S. Cui, X. Zhang, T.-l. Liu, J. Lee, D. Bracher, K. Ohno, D. Awschalom, and E. L. Hu, "Hybrid plasmonic photonic crystal cavity for enhancing emission from near-surface nitrogen vacancy centers in diamond," ACS Photonics **2**, 465–469 (2015).
[43]H. Son, T. Choi, K. Kim, Y. Kim, J. Bang, S.-J. Kim, B. Lee, and Y. Jeong, "Strong coupling induced bound states in the continuum in a hybrid metal–dielectric bilayer nanograting resonator," ACS Photonics **11**, 3221–3231 (2024).
[44]A. Sarto Polo and K. Passalacqua Morelli Frin, "Fundamentals of photochemistry: Excited state formation/deactivation and energy transfer processes," in *Springer Handbook of Inorganic Photochemistry* (Springer, 2022), pp. 27–48.
[45]T. Schnappinger, D. Jadoun, M. Gudem, and M. Kowalewski, "Time-resolved X-ray and XUV based spectroscopic methods for nonadiabatic processes in photochemistry," Chem. Commun. **58**, 12763 (2022).
[46]B. Le Dé, S. Huppert, R. Spezia, and A. W. Chin, "Extending non-perturbative simulation techniques for open-quantum systems to excited-state proton transfer and ultrafast non-adiabatic dynamics," J. Chem. Theory Comput. **2024**, 8749.
[47]H.-P. Breuer and F. Petruccione, *The Theory of Open Quantum Systems* (Oxford University Press, 2002).
[48]G. Grynberg, A. Aspect, and C. Fabre, *Introduction to Quantum Optics: From the Semi-classical Approach to Quantized Light* (Cambridge University Press, 2010).
[49]I. Medina, F. J. García-Vidal, A. I. Fernández-Domínguez, and J. Feist, "Few-mode field quantization of arbitrary electromagnetic spectral densities," Phys. Rev. Lett. **126**, 093601 (2021).
[50]S. I. Bozhevolnyi and J. B. Khurgin, "Fundamental limitations in spontaneous emission rate of single-photon sources," Optica **3**, 1418 (2016).

[51] J. Fait, S. Putz, G. Wachter, J. Schalko, U. Schmid, M. Arndt, and M. Trupke, "High finesse microcavities in the optical telecom O-band," Appl. Phys. Lett. **119**, 221112 (2021).
[52] R. Loudon, *The Quantum Theory of Light* (OUP Oxford, 2000).
[53] N. Moiseyev, S. Scheit, and L. S. Cederbaum, "Non-hermitian quantum mechanics: Wave packet propagation on autoionizing potential energy surfaces," J. Chem. Phys. **121**, 722–725 (2004).
[54] A. Ben-Asher and N. Moiseyev, "The boomerang effect in electron-hydrogen molecule scattering as determined by time-dependent calculations," J. Chem. Phys. **146**, 204303 (2017).
[55] A. Ben-Asher, A. Landau, L. S. Cederbaum, and N. Moiseyev, "Quantum effects dominating the interatomic coulombic decay of an extreme system," J. Phys. Chem. Lett. **11**, 6600–6605 (2020).
[56] F. Roccati, G. M. Palma, F. Ciccarello, and F. Bagarello, "Non-Hermitian physics and master equations," Open Syst. Inf. Dyn. **29**, 2250004 (2022).
[57] G. Lindblad, "On the generators of quantum dynamical semigroups," Commun. Math. Phys. **48**, 119–130 (1976).
[58] N. Moiseyev, *Non-Hermitian Quantum Mechanics* (Cambridge University Press, 2011).
[59] A. D. Isaacson and K. Morokuma, "Molecular orbital studies of hydrogen bonds. VIII. Malonaldehyde and symmetric hydrogen bonding in neutral species," J. Am. Chem. Soc. **97**, 4453–4457 (1975).
[60] G. Karlstrom, H. Wennerstrom, B. Jonsson, S. Forsen, J. Almlof, and B. Roos, "Intramolecular hydrogen bond. ab initio MO calculations on the enol tautomer of malondialdehyde," J. Am. Chem. Soc. **97**, 4188–4192 (1975).
[61] B. A. Ruf and W. H. Miller, "A new (Cartesian) reaction-path model for dynamics in polyatomic systems, with application to H-atom transfer in malonaldehyde," J. Chem. Soc., Faraday Trans. 2 **84**, 1523–1534 (1988).
[62] J. P. P. Zauleck, S. Thallmair, M. Loipersberger, and R. de Vivie-Riedle, "Two new methods to generate internal coordinates for molecular wave packet dynamics in reduced dimensions," J. Chem. Theory Comput. **12**, 5698–5708 (2016).
[63] J. P. P. Zauleck and R. de Vivie-Riedle, "Constructing grids for molecular quantum dynamics using an autoencoder," J. Chem. Theory Comput. **14**, 55–62 (2018).
[64] J.-D. Chai and M. Head-Gordon, "Long-range corrected hybrid density functionals with damped atom–atom dispersion corrections," Phys. Chem. Chem. Phys. **10**, 6615–6620 (2008).
[65] R. A. Kendall, T. H. Dunning, Jr., and R. J. Harrison, "Electron affinities of the first-row atoms revisited. systematic basis sets and wave functions," J. Chem. Phys. **96**, 6796–6806 (1992).
[66] M. J. Frisch, G. W. Trucks, H. B. Schlegel, G. E. Scuseria, M. A. Robb, J. R. Cheeseman, G. Scalmani, V. Barone, G. A. Petersson, H. Nakatsuji, X. Li, M. Caricato, A. V. Marenich, J. Bloino, B. G. Janesko, R. Gomperts, B. Mennucci, H. P. Hratchian, J. V. Ortiz, A. F. Izmaylov, J. L. Sonnenberg, D. Williams-Young, F. Ding, F. Lipparini, F. Egidi, J. Goings, B. Peng, A. Petrone, T. Henderson, D. Ranasinghe, V. G. Zakrzewski, J. Gao, N. Rega, G. Zheng, W. Liang, M. Hada, M. Ehara, K. Toyota, R. Fukuda, J. Hasegawa, M. Ishida, T. Nakajima, Y. Honda, O. Kitao, H. Nakai, T. Vreven, K. Throssell, J. A. Montgomery, Jr., J. E. Peralta, F. Ogliaro, M. J. Bearpark, J. J. Heyd, E. N. Brothers, K. N. Kudin, V. N. Staroverov, T. A. Keith, R. Kobayashi, J. Normand, K. Raghavachari, A. P. Rendell, J. C. Burant, S. S. Iyengar, J. Tomasi, M. Cossi, J. M. Millam, M. Klene, C. Adamo, R. Cammi, J. W. Ochterski, R. L. Martin, K. Morokuma, O. Farkas, J. B. Foresman, and D. J. Fox, *Gaussian 16 Revision C.01*, Gaussian Inc., Wallingford, CT, 2016.
[67] S. Hirata and M. Head-Gordon, "Time-dependent density functional theory within the Tamm–Dancoff approximation," Chem. Phys. Lett. **314**, 291–299 (1999).
[68] M. Kowalewski and P. Seeber, "Sustainable packaging of quantum chemistry software with the Nix package manager," Int. J. Quantum Chem. **122**, e26872 (2022).
[69] B. Podolsky, "Quantum-mechanically correct form of Hamiltonian function for conservative systems," Phys. Rev. **32**, 812–816 (1928).
[70] E. B. Wilson, J. C. Decius, and P. C. Cross, *Molecular Vibrations: The Theory of Infrared and Raman Vibrational Spectra* (Dover Publication, 1980).
[71] L. Schaad and J. Hu, "The Schrödinger equation in generalized coordinates," J. Mol. Struct.: THEOCHEM **185**, 203–215 (1989).
[72] S. Thallmair, M. K. Roos, and R. de Vivie-Riedle, "Design of specially adapted reactive coordinates to economically compute potential and kinetic energy operators including geometry relaxation," J. Chem. Phys. **144**, 234104 (2016).
[73] J. Feist, A. I. Fernández-Domínguez, and F. J. García-Vidal, "Macroscopic qed for quantum nanophotonics: Emitter-centered modes as a minimal basis for multiemitter problems," Nanophotonics **10**, 477–489 (2020).
[74] A. A. R. Garcia, C.-A. Mao, and W.-H. Cheng, "Realization of ultrastrong coupling between LSPR and Fabry–Pérot mode via self-assembly of Au-NPs on p-NiO/Au film," Nanophotonics **13**, 2501–2512 (2024).
[75] K. Georgiou, P. Michetti, L. Gai, M. Cavazzini, Z. Shen, and D. G. Lidzey, "Control over energy transfer between fluorescent bodipy dyes in a strongly coupled microcavity," ACS Photonics **5**, 258–266 (2018).
[76] F. Barachati, J. Simon, Y. A. Getmanenko, S. Barlow, S. R. Marder, and S. Kéna-Cohen, "Tunable third-harmonic generation from polaritons in the ultrastrong coupling regime," ACS Photonics **5**, 119–125 (2018).
[77] A. Ben-Asher, A. I. Fernández-Domínguez, and J. Feist, "Memory loss is contagious in open quantum systems," arXiv:2402.16096 (2024).